

A Thermal Modelling Approach and Experimental Validation for an Oil Spray-Cooled Hairpin Winding Machine

Fengyu Zhang, David Gerada, *Senior Member, IEEE*, Zeyuan Xu, Chuan Liu, He Zhang, *Senior Member, IEEE*, Tianjie Zou, Yew Chuan Chong, Chris Gerada, *Senior Member, IEEE*

Abstract—While the electromagnetic aspects of hairpin windings are actively being investigated and discussed in recent literature, including the design rules together with the loss calculation and reduction techniques, the thermal performance and modeling aspects have received less attention to date. In hairpin windings, the conductors (pins) are comparatively larger and arranged as separate components in parallel within the slot. In contrast, conductors randomly overlap and contact each other for traditional random windings. The differences in the aforementioned winding physical characteristics result into a different methodology to develop the thermal network. This paper presents a 3D Lumped Parameter Thermal Network (LPTN) approach for an oil-spray cooled hairpin winding, which includes the slot thermal model configuration, the end-winding connections, together with different methodologies of analyzing the end-winding sprayed-oil characteristics. The aforesaid thermal model captures unique features related to the winding technology and cooling mechanism, such as the non-uniform end-winding temperature caused by the uneven oil spray cooling effects. Finally, taking an existing propulsion drive hairpin stator and a bespoke-designed test setup, the presented steady state thermal modelling approach is experimentally validated covering various experimental tests, including different spray conditions.

Index Terms—Hairpin winding, propulsion, oil spray, thermal network, end-winding, steady state

I. INTRODUCTION

WITH the requirements of high efficiency, high power density (kW/kg or kW/L) together with the equally important cost performance (\$/kg) for transportation applications, motors with higher operational current densities

Manuscript received October 24, 2020; revised February 7, 2021; accepted March 4, 2021. This work was supported in part by the Clean Sky 2 Joint Undertaking under the European Union’s Horizon 2020 research and innovation programme under grant agreement number 821399 and Motor Design, Ltd. (*Corresponding author: David Gerada*)

F. Zhang, D. Gerada, Z. Xu, C. Liu, T. Zou, C. Gerada are with the Power Electronics, Machines and Control group, University of Nottingham, Nottingham, NG7 2 RD, UK (e-mail: Fengyu.Zhang@nottingham.ac.uk; David.Gerada@nottingham.ac.uk; Zeyuan.xu@nottingham.ac.uk; Chuan.liu2@nottingham.ac.uk; Tianjie.zou@nottingham.ac.uk; Chris.Gerada@nottingham.ac.uk).

H. Zhang is with the Key Laboratory of More Electric Aircraft Technology of Zhejiang Province, University of Nottingham Ningbo China, Ningbo 315100, China (email: He.Zhang@nottingham.edu.cn)

Y. Chong is with Motor Design, Ltd., Wrexham, UK (email: Eddie.Chong@motor-design.com)

and with enhanced cooling techniques are currently active research and development topics [1, 2]. Besides the developments in electromagnetic and thermal aspects, efficient manufacturing is also a big source of entitlement for making stronger electrification business cases. Hairpin windings are increasingly being adopted in traction motors due to their reduced manufacturing time [3] and specific advantages such as the uniformity/accuracy in conductor placement [4, 5], which eliminates the uncertainties in both the AC losses as well as the end-winding shape, allowing for the design of more reliable cooling systems [6-8]. Furthermore the copper fill factor is almost doubled with respect to the traditional random windings, which further helps with improving the overall performance metrics [9, 10]. The procedure of designing a hairpin stator is described in [11-13] including different winding design options and connection patterns.

For traditional random-wound motors, with high stator winding losses, water jacket cooling around the stator periphery is more efficient compared to air cooling [14], and is reliably used in many high Technology Readiness Level applications. Novel cooling topologies, such as slot water jacket cooling targeting the heat generated inside the slot directly are also an efficient way for reducing winding temperature, albeit the increased copper losses [15, 16]. With the aforementioned cooling techniques, the concern and investigation on the end-winding heat transfer arises. Oil-spray cooling in the end-winding region is investigated in [17, 18], highlighting its effectiveness. Local winding temperature analysis is performed and plotted as a function of both the oil flow-rate and rotor speed, indicating that the rotational speed influence is less sensitive on the winding temperatures compared to the oil flow rate [17]. However, the oil convection heat transfer is not quantified in this study, which is subsequently addressed by [19, 20], with the heat transfer coefficient (HTC) investigated and plotted as a function of the spray parameters, such as nozzle height, inlet pressure, sub-cooling and spraying angle. Nevertheless, in the aforementioned studies, the thermal behavior of the sprayed end-winding in an actual spray-cooled machine is not modeled and the complicated end-winding heat transfer characteristics are heavily simplified due to (i) end-windings’ complex geometry; (ii) the uneven temperature distribution in the end-winding region for different slots. There are research approaches to tackle the problems related to complicated end-winding geometry for air-cooled machines in [21-23] using empirical formulas and for directly cooled machines using CFD analysis [24, 25]. In these works the temperature distribution at the end-winding region is assumed

uniform along the end-winding circumference. However, with oil-spray cooling the situation is more complex, as the cooling effects on different sections of the end-winding are quite dissimilar, which results in a significantly uneven temperature distribution for the end-winding [17]. The thermal modelling at a machine level to consider the uneven temperature distribution in the end-winding caused by the sprayed-cooling effects is not investigated within any of the existing literature.

LPTN thermal models are widely used due to their quick solving characteristics and are a mature tool in the thermal modeling of motors with traditional random windings [26-29]. Exploiting motor symmetries, the motor part corresponding to half a stator slot is simulated and validated [14]. For the thermal model, the effective thermal conductivity is applied to obtain the slot thermal condition [22] and empirical formulae are derived based on the fluid characteristics in the air-gap/end-winding region [21]. However, inaccurate temperature distribution and hot spot temperature prediction will result if the aforesaid traditional simplified half-slot symmetry models are used to conduct thermal analysis on machines with oil-spray cooling due to the uneven temperature distribution in the end-winding region.

The contributions of this paper are as follows:

1) A thermal approach to analyze the hairpin winding thermal behavior is proposed, which highlights the differences between a classic random wound machine and a hairpin winding machine. This is especially so for the slot thermal conditions together with the important coupling between electrical connections and the thermal aspects of the electrical machine.

2) The heat transfer coefficient and convection area formulas are derived and presented in this paper for the uneven heat transfer characteristics in the end-winding region due to the sprayed cooling effects. The proposed methodologies are applicable to any form of thermal analysis, including, LPTN, FEA, CFD, and to any general motor setup employing a sprayed cooling system.

3) A LPTN model is built which considers point 1) and 2) above. This is experimentally validated on a specially designed test rig with a hairpin winding stator.


The paper is organized as follows: in section II, the thermal model of the whole hairpin-winding stator is presented, including the modelling technique and the thermal model parameters selection. In section III, the convection heat transfer which captures the uneven temperature distribution caused by the sprayed-oil in the end-winding region is detailed for the thermal network, including the heat transfer coefficient and convection area calculation. Using a bespoke-developed test-rig, the results of the thermal model are experimentally validated when the test rig runs to steady state in section IV. Finally, conclusions from this research are summarized in section V.

II. THERMAL MODELLING OF HAIRPIN WINDING

A 3D thermal network based on an existing hairpin-wound stator is developed in this section, describing the methodologies and specific considerations. For reference the key formulas of this network are included in the Appendix section of this paper. The stator investigated in this paper is an off-the-shelf Delco-

Remy HVH250 machine featuring a 2-layer hairpin winding configuration, with parameters listed in TABLE I.

TABLE I. Hairpin winding stator used in this research

Outer diameter	215 mm	
Inner diameter	160 mm	
Active length	60 mm	
Cooling Type	Oil-spray cooled	
Winding type	Hairpin winding	
Layer number	Two	
Pin dimensions	3mm × 4mm	
Slot dimensions	4mm × 12mm	

A. Lumped Parameter Thermal Network (LPTN) of hairpin winding machine

The thermal network for machines with traditional windings considers the periodic and symmetrical geometry of machine, and typically only a half slot or one slot is modeled for reducing computation time [14]. There are different types of LPTN developed for traditional winding in recent literature: (Type ‘i’) different number of nodes are selected based on the balance between the results’ accuracy and the computational speed [30]; (Type ‘ii’) simplified thermal model using cuboidal element method or ‘T’ type using average temperature in the slot [31, 32]; (Type ‘iii’) nodes with improved power losses are investigated in [33, 34]. Both the aforementioned methods require the determination of the equivalent slot thermal conductivity, considering all slot constituent materials, including copper, wire insulation, as well as the impregnation resin.

However, since in the LPTN developed for the electrical machines equipped with hairpin winding there are a small number of conductors placed in the slot compared to the traditionally wound machine, it is practical to model each individual conductor with one node without incurring time penalties. Furthermore since the conductor has a high thermal conductivity, the temperature gradient across the conductor area is small and thus a low node number with one node per conductor does not decrease LPTN model accuracy. Oil sprayed cooling is commonly used in hairpin winding electrical machines, which results in an uneven temperature distribution in the end-winding region and also in considerable axial heat transfer along the high thermal conductivity conductor. Therefore, in this paper, a 3D full-slot LPTN model is proposed on an oil-spray cooled hairpin winding featuring multiple nozzles.

In the 3D thermal network, the temperature of a hairpin conductor is considered to be constant within its cross-section, with the number of nodes in the radial direction of the slot determined by the conductor layer number per slot, i.e. two in this case study. The two layers of hairpin winding are geometrically in parallel inside the slot, i.e. an upper conductor and a lower conductor for each slot, as shown in Fig. 1. This figure presents an example of the radial thermal network for two adjacent slots, where the gaps between the conductors themselves and between the conductors and stator core are

exaggerated for illustrative purposes. It is also worth noting that the thermal resistance of the insulation material (enamel) that surrounds the copper is also included.

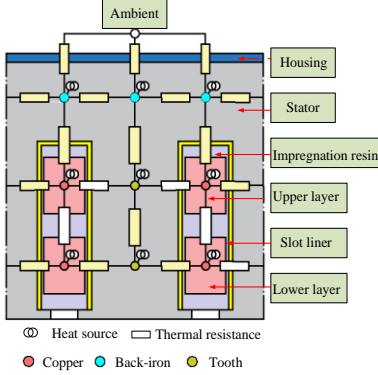


Fig. 1. Radial thermal network

The axial thermal network connecting three adjacent radial planes and two corresponding end-winding planes is shown in Fig. 2. Differently to traditional windings with crossed and twisted conductors, there are accurately defined gaps between the upper and lower layer conductors, and also between the conductors from any neighboring slots in the end-winding region as shown in Fig. 3. These enable all conductors to be directly cooled by oil droplets from the sprayed oil.

Only the ‘oil-sprayed end’ of the machine as shown on the left side of Fig. 2 is equipped with sprayed oil, while the right side (or ‘non-sprayed end’) of the stator is enclosed and dry. In the thermal network, on the non-sprayed-end, fluid (air) temperature is then considered evenly distributed. Meanwhile, the convection heat transfer between the fluids and the stator back-iron and teeth are also considered and applied to the thermal network [21].

The convection heat transfer between the two hairpin windings from the same slot and the fluid is considered independent, with the resistances shown in Fig. 2 colored by — and — representing the thermal resistance between the fluid and the upper layer winding, while the resistances colored by — and — represent the thermal resistance between the fluid and the lower layer winding.

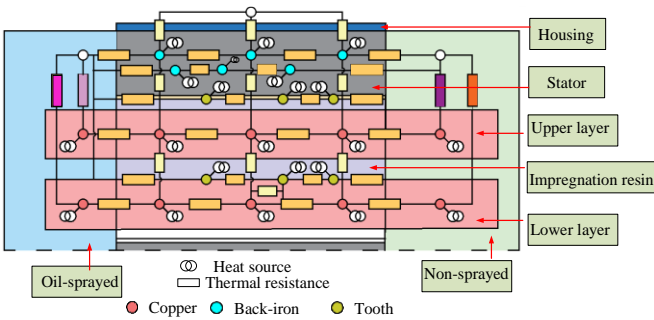


Fig. 2. Axial thermal network (double layer configuration)

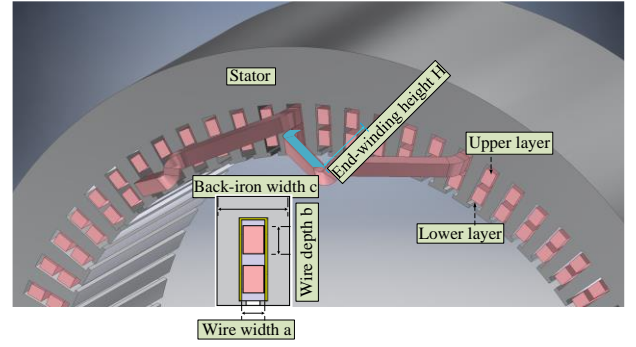


Fig. 3. An example of end-winding connection

B. Correlation between electrical connection and thermal network

In this paper, for hairpin windings, thermal paths of the end-windings from different slots follow the same connection patterns as with the electrical connections between the three phases. In constructing the thermal network it is, therefore, important to map out each hairpin’s electrical connections to describe the physical connections in the end-winding region. Fig. 3 is an example of the physical (and thermal/electrical) connection corresponding to the motor case-study in TABLE I, where the same conductor is crossing across six slots on one side.

Fig. 4 plots a map of hairpin stator electrical connections for one phase and also the corresponding thermal resistances at both the non-sprayed and the oil-sprayed sides are shown. The winding for the phase shown in Fig. 4, starts from the upper winding in slot 8 and ends in the bottom winding in slot 68, as indicated by the (○) within these slots. The solid fill (■) resistances represent the thermal resistances on the oil-sprayed side, while the hollow-fill (□) resistances represent those on the thermally insulated (i.e. non-sprayed-oil) side. Lines in different colors (—, —, —, —) represent one single conductor, with the solid lines representing the conductor on the oil-sprayed side, while the dashed lines represent the conductor on the non-sprayed side. Conductor axial thermal resistances for the straight section (i.e. within the slot/core) are not shown on purpose, in order to give a clear view of the end-winding thermal connections.

The connections between one node and the adjacent nodes (‘n’ nodes in total) in the described LPTN are built with the heat conservation equation (1):

$$q_i + \sum_{j \neq i}^n \frac{T_j - T_i}{R_{ij}} = 0 \quad (1)$$

where ‘ R_{ij} ’ is the thermal resistance between node ‘ i ’ and node ‘ j ’, while node temperature is represented by ‘ T_i ’, ‘ T_j ’, respectively. In equation (1) ‘ n ’ represents the total number of nodes that are adjacent to the ‘ i ’ node, while ‘ q_i ’ is the heat loss generated in node ‘ i ’. For this research which focuses

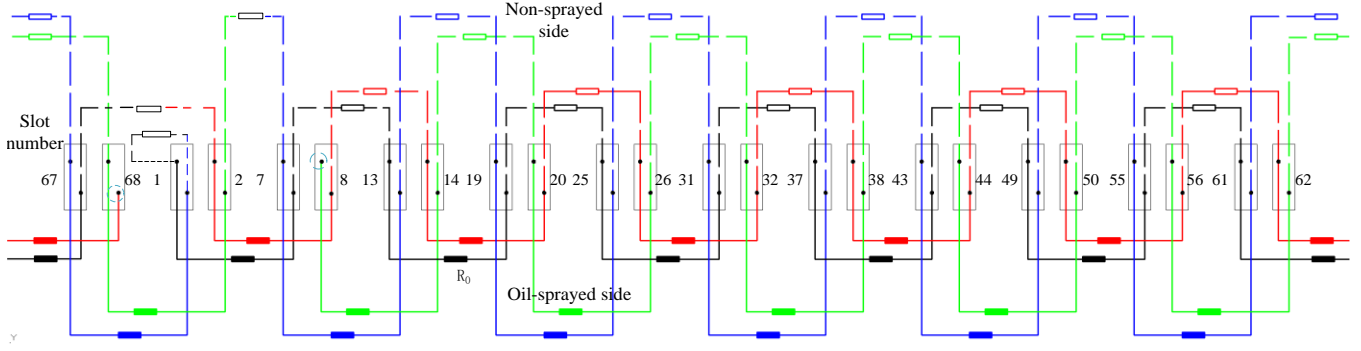


Fig. 4. Electrical connections and corresponding thermal resistance map for one phase (2 slots per pole per phase)

specifically on the thermal modelling, only DC copper losses are considered. This assumption, as in previous similar research [14], for the purpose of thermal model validation is considered valid, since next generation high power density machines are copper loss dominant [2], and furthermore the main effect of the winding AC copper losses would be to increase the copper loss magnitude, hence increasing the dominance of copper losses [13, 35]. The additional copper losses from AC effects in hairpin windings are predominantly concentrated on the periphery of the conductor due to skin effect which in a way makes their heat removal by spray cooling easier.

Furthermore, only thermal conduction within the solid parts together with convection at the end-winding region are considered, while any heat dissipation by radiation is ignored. In general, thermal conduction resistances are described with:

$$R = x/kA_{cross} \quad (2)$$

where 'x' is the distance between adjacent nodes along the heat flow, ' A_{cross} ' is the cross-sectional area which is perpendicular to the heat flow, while 'k' is the material thermal conductivity between the two nodes and is determined as follows for different parts in the stator. The stator lamination thermal conductivity is 30 W/(m·K) and 0.87 W/(m·K) in the radial and axial planes respectively. Differently from the traditional windings, where an equivalent thermal conductivity is typically used in the slot (0-2 W/(m·K)) [36], for hairpin windings the actual copper thermal conductivity value (401 W/(m·K)) is used in the thermal network for the conductors in slot. The impregnation (EpoxyLite TSA220) thermal conductivity is 0.21 W/(m·K) while the slot liner (Nomex 410) thermal conductivity is 0.17 W/(m·K).

Convection heat transfer occurs mainly in two places, (i) between the housing and ambient air; (ii) in the end-winding region. Equation (3) is used to calculate the convection thermal resistance:

$$R = 1/hA_{conv} \quad (3)$$

where 'h' is the heat transfer coefficient, and ' A_{conv} ' is the effective convection area. For convection heat transfer between housing and ambient air, ' A_{conv} ' corresponds to the surface area of the housing frame, while 'h' is the natural convection heat transfer coefficient with the experimental values adopted from [37]. For convection occurs in the end-winding region, 'h' is determined by the experimental results as detailed in section III.

III. CONVECTION HEAT TRANSFER IN END-WINDING REGION

This section presents in detail the methodologies to deal with the convection heat transfer between the sprayed-oil and the end-winding. Part A describes the equivalent convection area calculation while the heat transfer coefficient calculation formulas are presented in part B. The combinations of different convection areas and heat transfer coefficient formulas are incorporated in the thermal model detailed earlier in section II for thorough experimental validation in section IV.

A. Equivalent convection area calculation

Due to the rectangular shape of the hairpin conductors and the nature of axially oriented sprayed-oil, only the surfaces facing to the sprayed-oil are directly impinged by the oil droplets and achieve a better cooling performance. On the other hand, for the conductor surfaces 'hidden' from the direct sprayed-oil flow (shaded in blue in Fig. 3), the cooling performance is somewhat weaker as it depends on the splashed oil droplets from the aforementioned 'direct' surfaces, which result into an oil mist flowing around the end winding. Furthermore, oil films, covering the conductor surfaces, also contribute to the cooling improvement of hairpin end-windings. Unfortunately, it is almost impossible to identify and separate all the aforesaid effects of the sprayed-oil cooling performance based on the experimental data of end-winding temperatures. Thus, in this work, an effective surface area coefficient ' β ' is introduced to reflect the effective convection area between the hairpin end-winding and the sprayed-oil, considering the effects of the impingement as well as the physical distance between the nozzle and the end-winding. This coefficient is then used to calculate the effective convection thermal resistance and is implemented into the thermal network model.

Based on different assumptions and levels of complexities, three methods are presented to calculate ' A_{conv} ' for the end-winding region in this paper, as per formulas (5) to (7).

$$A_{end} = (2a + 2b) \times l \quad (4)$$

$$A_1 = A_{end} \quad (5)$$

$$A_2 = \beta_0 \times A_{end} \quad (6)$$

$$A_3 = \beta \times A_{end} \quad (7)$$

$$l = H + 3c \quad (8)$$

In the most basic form, when $A_{conv} = A_1$, it is assumed that the effective convection area is the total surface area of the hairpin conductor ' A_{end} ' (i.e., the entire blue-shaded area of Fig. 3 is also considered to be impinged by the sprayed-oil). In this case ' A_1 ' is same as ' A_{end} ', calculated by multiplying the perimeter (profile) of the rectangular bar by half the arithmetic end-winding length ' l ' as described by equations (4), (8). In these equations, referring to Fig. 3, ' a ', ' b ' are the conductor width and depth respectively, ' c ' is the distance between the centers of two adjacent slots, while ' H ' is the end-winding height.

From the foregoing description of ' A_1 ', it can be understood that this is an optimistic (best-case) scenario. An opposite assumption can be made that one side of the conductor is entirely hidden from the benefits of spray cooling (i.e. blue side of Fig. 3 is dry), which corresponds to the effect represented by the coefficient β_0 in equation (6), for which $A_{conv} = A_2$. In this case it follows that the coefficient β_0 is formulated from the ratio of three conductor sides to the entire conductor perimeter as described by equation (9).

$$\beta_0 = (a + 2b)/(2a + 2b) \quad (9)$$

For the case in hand, considering the pin dimensions, β_0 is equal to 0.7857.

The third and last approach for the determination of the effective convection area, $A_{conv} = A_3$, relies on using measured data to modify the convection area between the sprayed-oil nozzle and the slot location for each individual hairpin conductor. This, therefore, considers the physical distance of the slot to the spray nozzles in the experiment. In this case the definition of ' β ' is based on the experimental data measured from the end-winding of different hairpin slots,

$$\beta = \frac{\beta_0(T_{ave} - T_{oil})}{T_{\#slot} - T_{oil}} \quad (10)$$

where ' T_{ave} ' is the measured average end-winding temperature, ' T_{oil} ' is the sprayed oil temperature, while ' $T_{\#slot}$ ' is the measured temperature specific to that slot. Details of measurement points are described in the experimental section IV.

B. Heat transfer coefficient calculation

The foregoing discussion dealt with the considerations and calculation methods for the effective convection area ' A_{conv} '. From equation (3), the other important aspect is the heat transfer coefficient ' h '. For this, again, three approaches are considered in this paper. In the simplest calculation, from the experimentally-measured data (end-winding temperature and heat input), the average heat transfer coefficient ' h_{ave} ' of all the end-winding is obtained as follows:

$$q = \frac{Q}{2 \times N} \quad (11)$$

$$h_{ave} = q/[A_{end}(T_{ave} - T_{oil})] \quad (12)$$

where ' q ' is the corresponding loss of a single conductor dissipated to the sprayed-oil, ' Q ' is the heat loss dissipated to the sprayed-oil (heat losses dissipated to the ambient environment have been excluded in the sprayed-oil experiment), ' N ' is the slot number (72 for the case in hand), while ' T_{ave} ' and ' T_{oil} ' are average conductor end-winding temperature and sprayed-oil temperature, respectively.

A second approach for the calculation of ' h ' which puts more resolution is suitable for the situation where nozzles are placed in symmetric locations and thus thermal conditions are approximately symmetrical (bar the effects of oil gravity) whilst exhibiting a degree of periodicity. To illustrate this, taking into account the motor in TABLE I, a case is investigated where 12 nozzles are evenly distributed circumferentially around the end-winding while they spray onto the end-winding in the axial direction, one at each hour position (using the clock positioning system), as described in Fig. 5. In such case, this figure shows that the end-winding area for six slots is covered by each nozzle. Taking into account the various symmetries, this results into four independent heat transfer coefficients (i.e., ' h_{ave1} ', ' h_{ave2} ', ' h_{ave3} ', ' h_{ave4} '), as shown in Fig. 5. TABLE II summarizes the heat transfer coefficients distribution on the oil-sprayed side for the end-winding region and formulas from (13) to (16) are used to calculate the average heat transfer coefficient. For example, ' h_{ave1} ' is calculated with (13), where ' T_i ' is the average temperature of conductors measured in slots shown in the second row of the TABLE II (i.e., slot#1, slot#7, ..., slot#67). Similarly, ' h_{ave2} ', ' h_{ave3} ' and ' h_{ave4} ', can be calculated from the slot numbers indicated in the same table.

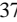
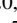
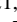

$$h_{ave1} = q/[A_{end}(\frac{\sum T_i}{12} - T_{oil})] \quad (13)$$

$$h_{ave2} = q/[A_{end}(\frac{\sum T_j}{24} - T_{oil})] \quad (14)$$

$$h_{ave3} = q/[A_{end}(\frac{\sum T_m}{24} - T_{oil})] \quad (15)$$

$$h_{ave4} = q/[A_{end}(\frac{\sum T_n}{12} - T_{oil})] \quad (16)$$

TABLE II. Average h distribution

average h		Slot#	Total slots
h_{ave1} , 	i	1, 7, 13, 19, 25, 31, 37, 43, 49, 55, 61, 67	12
h_{ave2} , 	j	2, 6, 8, 12, 14, 18, 20, 24, 26, 30, 32, 36, 38, 42, 44, 48, 50, 54, 56, 60, 62, 66, 68, 72	24
h_{ave3} , 	m	3, 5, 9, 11, 15, 17, 21, 23, 27, 29, 33, 35, 39, 41, 45, 47, 51, 53, 57, 59, 63, 65, 69, 71	24
h_{ave4} , 	n	4, 10, 16, 22, 28, 34, 40, 46, 52, 58, 64, 70	12

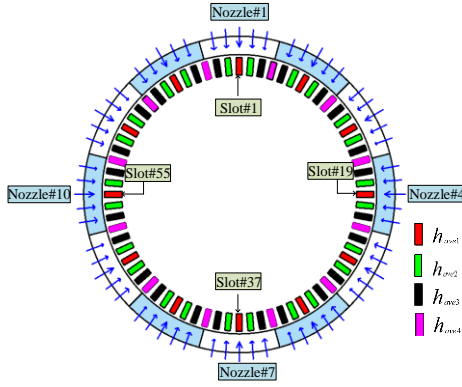


Fig. 5. Heat transfer coefficient on the oil-sprayed side

The third approach for the calculation of ‘ h ’, calculates the local ‘ h ’ for each single conductor, in which the case ‘ T_{ave} ’ in equation (12) is replaced by the local temperature ‘ $T_{\#slot}$ ’, as in equation (17),

$$h_{\#slot} = q/[A_{end}(T_{\#slot} - T_{oil})] \quad (17)$$

C. Methodologies of end-winding oil-spray simulation

Based on the foregoing discussions for the calculation of ‘ A_{conv} ’ and ‘ h ’, thermal networks are developed with four methodologies to represent the convection heat transfer for the oil-sprayed end-winding region, as detailed in TABLE III. The thermal network with all the aforementioned end-winding methodologies will be applied to different case studies and compared to experimental results in section IV.

TABLE III. Four methodologies of end-winding oil-spray simulation in the thermal network

End-winding methodology	h	A_{conv}
#i	h_{ave} in (12)	$A_{conv} = A_1 = (2a + 2b) \times l$
#ii	$h_{ave1}, h_{ave2}, h_{ave3}, h_{ave4}$	$A_{conv} = A_2 = \beta_0 \times (2a + 2b) \times l$
#iii	Single conductor local $h_{\#slot}$	$A_{conv} = A_3 = \beta \times (2a + 2b) \times l$
#iv		

IV. EXPERIMENTAL VALIDATION

Using a bespoke-developed test rig shown in Fig. 6, the thermal network of the preceding section is validated experimentally using two approaches: (i) natural convection, where housing in Fig. 6 is exposed to the ambient air; and (ii) oil-sprayed cooling, where the end-windings on the ‘oil-sprayed end’ in Fig. 2 are exposed to the sprayed oil, and the full test rig casing is thermally insulated from the ambient environment using 6mm-thick Calcium-Magnesium-Silicate sheets in order to minimize the uncertainty factors of the convection heat transfer between the test rig and ambient environment. The hairpin winding is heated by a DC current from the power supply shown, while the generated losses are removed by sprayed-oil onto the hairpin end-windings. Twelve

(12) nozzles, one at each hour position, are installed on the machine front end-flange as shown in Fig. 6, and are used for generating axial sprayed-oil on the oil-sprayed side. A data logger is used to record the temperatures from the multiple ‘K’ type thermocouples, which are directly attached to the winding and covered by a thin layer of insulation.

Thermocouples are located on both layers of the oil-sprayed end-winding region in order to capture a full image of the temperature distribution, as shown in Fig. 7. In this figure, the green and red colors denote thermocouples placed on the upper and lower layers respectively.

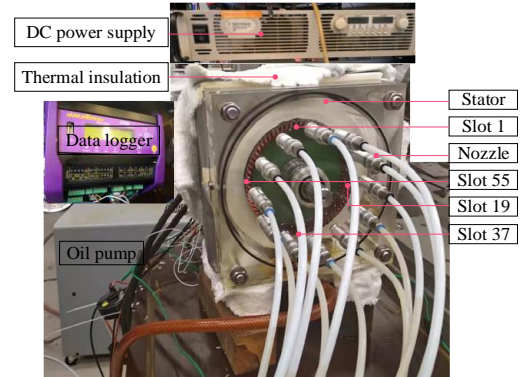


Fig. 6. Test rig

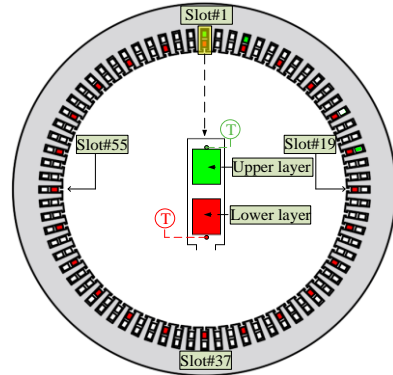


Fig. 7. Thermocouple locations

A. Natural convection experimental validation

Natural convection tests are performed in order to validate the thermal network model of section II under a simple cooling condition. For the case of natural convection, air in the enclosed end-winding region is driven by buoyancy only, hence the cooling performances for all end-winding conductors are similar and uniform. Heat generated in the conductors is conducted to the machine housing and then dissipated to the ambient air by natural convection. In Fig. 8, the average end-winding temperature is plotted versus the input current, with (■) and (--) denoting the experimental and simulation results, respectively. The experimental data agrees well with the simulation results, with acceptable deviation mainly due to the thermocouple location accuracy.

The thermal resistances model developed in the thermal network, including those radially, axially, as well as the inter-connections in the end-winding region are validated with the

natural convection experiment, with natural convection heat transfer coefficients obtained on the machine in the lab environment. The natural convection experiment is conducted in a large enclosed room with a controlled DC current applied to the winding in the absence of any active cooling. Environment temperature, machine winding as well as housing temperatures are monitored until a thermal steady condition is reached, at which point all the heat generated within the windings is dissipated via natural convection to the air surrounding the test section. The average heat transfer coefficient at the test section surface can be obtained from (18). In (18), ' $h_{natural}$ ' is the average natural heat transfer coefficient, ' Q_{rig} ' is the heat input to the winding, ' A_{rig} ' is the total surface area of the housing, ' $T_{housing}$ ', ' $T_{ambient}$ ' are the housing temperature and the ambient environment temperature, respectively, with the data listed in TABLE IV. The heat transfer coefficient used in the modelling is $6.2 \text{ W}/(\text{m}^2\cdot\text{K})$.

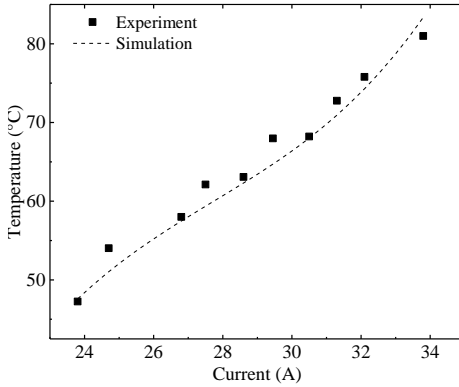


Fig. 8. Average end-winding temperature distribution for natural convection

$$h_{natural} = Q_{rig} / [A_{rig}(T_{housing} - T_{ambient})] \quad (18)$$

TABLE IV. Natural convection experimental results

Current	Voltage	Power losses	Housing temperature	Ambient temperature	Convection area	Heat transfer coefficient
A	V	W	°C	°C	m ²	W/(m ² ·K)
23.8	0.89	21.14	39.77	20	0.1743	6.1
28.6	1.18	33.68	51.27	20		6.2
33.8	1.48	49.86	64.5	20		6.4

B. Prediction of axial oil-spray cooling experiments

For forced sprayed-oil (BP Turbo Oil 2389, 40 °C) to the stator, various oil flow rates for the full test rig ranging from 2.40L/min to 3.53L/min and a 90.8A current are applied to validate the thermal network model described in section II. In this section, firstly, the temperature difference between the two winding layers is discussed, followed by the temperature variation with the slot number and oil flow rate. In the final part, simulation and experimental results comparisons are presented for the purpose of thermal network model validation, involving

the four cases shown in TABLE V. For each case, the thermal network with the four end-winding methodologies presented earlier in TABLE III are applied and compared.

TABLE V. Experimental cases studied for thermal model validation

Case	Experiment				LPTN with end-winding simulation : (refer to Table III)
	Nozzle type				
	Outlet diameter	Spray angle	Spray pattern	Nozzle number	
Case I	0.71 mm	75°	full-cone	12 (high flow rate)	#i, #ii, #iii, iv
Case II				12 (low flow rate)	
Case III				6	
Case IV	0.508 mm	120°	hollow-cone	12	

In the first instance the temperature difference between the two conductor layers (i.e., upper layer and lower layer) is investigated in correlation with the oil flow rate for slot#1, slot#4 and slot#16. The cooling effects on the two layers for the different slots are almost the same across the range of oil flow rates considered, with a maximum discrepancy of 10% observed from the experimental tests. In light of this, for the sake of clarity while still maintaining accuracy, only the lower layer conductor in the slot is plotted and analyzed hereafter.

Fig. 9 shows a close up view of the oil spray phenomenon in a configuration with twelve full-cone nozzles evenly applied to the end-winding, and Fig. 10 shows experimentally measured results of end-winding temperature for different slots under varying oil flow rates. Uneven temperatures are observed from different slots, which highlights that the thermal performance is different for each slot due to the nature of sprayed-oil cooling. At the locations from 10 o'clock to 2 o'clock (slot#60 to slot#10), the heat transfer rate values are smaller compared to the other locations due to gravity effects, which result in higher winding temperatures in this region. While the temperature pattern is similar for different flowrates, the temperature variation range increases as the flowrate reduces.



Fig. 9. Oil spray testing for case I with 50mm distance between the nozzle and the target surface

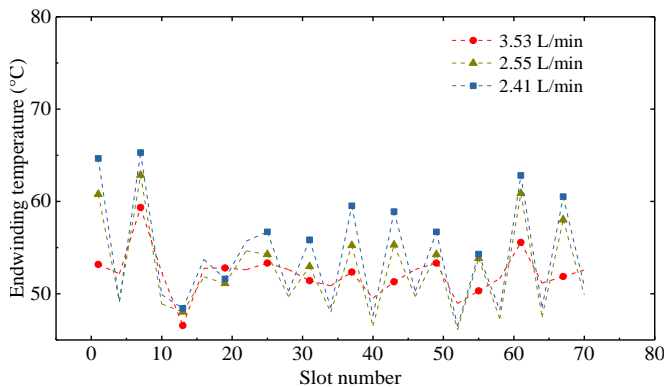


Fig. 10. Experimental temperature distribution for different slot numbers

As shown in TABLE V, the thermal network with four end-winding methodologies (i.e., #i, #ii, #iii, #iv) developed in section III is applied to experimental cases I and II, both having 12 evenly distributed full-cone nozzles. In Case I, shown in Fig. 11, a higher flowrate (3.5L/min) is used, while for Case II, corresponding to Fig. 12, the flowrate is reduced down to 2.4L/min. For both the aforesaid flow rates, Fig. 11 and Fig. 12, show that the predicted end-winding temperature with methodology ‘#i’, plotted with (---) is similar across all the slot numbers. This is understandable given that a uniform heat transfer coefficient in the end-winding region is assumed in this methodology, and therefore uniform winding temperature distribution is obtained at each slot. This method does not reflect the measured temperature profile which follows pulsating cycles corresponding to the setup of 12 equally-distributed nozzles over 72 slots.

The thermal network with end-winding methodology ‘#ii’ (---), where the heat transfer coefficient is repeating periodically over four slots as indicated in TABLE III, follows the experimental data pattern, with some differences which can be rooted to the local phenomena which are not modelled in this case, such as the gravity effects. As shown in TABLE VI, which tabulates key comparative data, the average temperature of the end-winding is slightly higher compared to that predicted with the thermal network with end-winding methodology ‘#i’, as the convection area becomes smaller with the area modification factor β_0 .

The contact area between the end-winding and the oil is modified in the thermal network with end-winding methodology ‘#iii’. The simulation results plotted with (---) provide a more accurate temperature profile, compared to the thermal network with end-winding methodology ‘#ii’. However, it should be borne in mind that with the repeating ‘average h ’ used, the impingement effects from oil spraying on heat transfer coefficient are captured only based on the physical distance of slot to the spray nozzles. Effects of oil film flows on the end-winding are not included, hence why the simulation pattern plotted by (---) follows the experimental data, though with larger deviations, compared to thermal network with end-winding simulation ‘#iv’.

Considering the oil gravity effects, which make the oil film thicker around the 4 to 8 o’clock locations (slots#25-#48), indeed when using single conductor local ‘ h ’, both Fig. 11 and

Fig. 12 indicate that the simulated end-winding temperatures agree quite well with the experimental data for the thermal network with end-winding methodology ‘#iv’, with small deviations. For reference, in case I with end-winding methodology ‘#iv’, the heat transfer coefficient is ranging from 212 W/m²K to 625 W/m²K, while the surface heat flux varies from 3610 to 5038 W/m² for different slots.

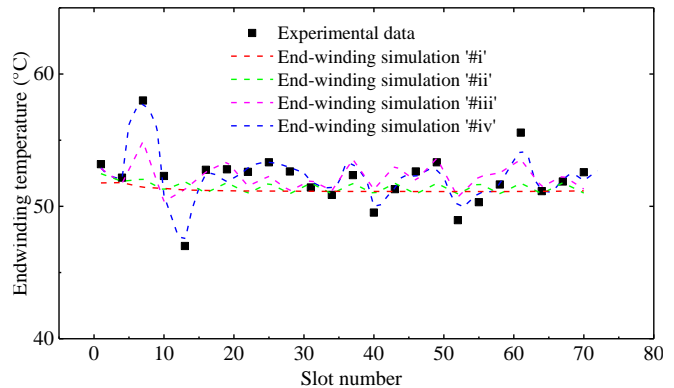


Fig. 11. Temperature comparison with case I for flow rate 3.53L/min

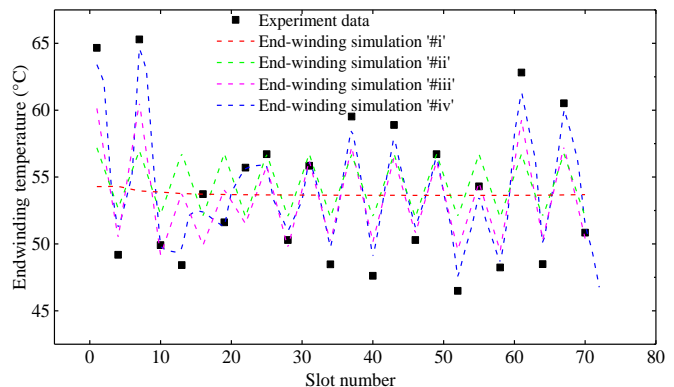


Fig. 12. Temperature comparison with case II for flow rate 2.4 L/min

To compare further the thermal model developed in section II A, experimental case III and case IV are performed considering different nozzle numbers and types. Fig. 13 presents the simulation and the experimental results for case III, featuring six full-cone nozzles evenly placed around the end-winding with a flow rate of 1.8L/min. In this case six temperature cycles are observed, and as in the previous two experimental plots, the temperature range is higher around the slots within the 10 o’clock to the 2 o’clock region where cooling performance is weaker due to oil gravity effects.

Similar to the previous cases, for case III both thermal networks with end-winding methodologies ‘#iii’ and ‘#iv’ provide a more accurate temperature profile, compared to the thermal networks with end-winding methodologies ‘#i’ and ‘#ii’. Finally, for experimental case IV, the 12 full-cone nozzles in case I are replaced by hollow-cone nozzles. Large temperature variations are observed in Fig. 14 at nozzle locations from 10 to 2 o’clock, similar to all the previous cases. However, there are no clear patterns of the temperature distribution with this type of nozzle. In fact, only the thermal network with end-winding methodology ‘#iv’ is able to deliver an accurate temperature profile, while the ability of the thermal network with end-winding methodologies ‘#i’, ‘#ii’ and ‘#iii’ is

limited, providing only an indication of the average winding temperature.

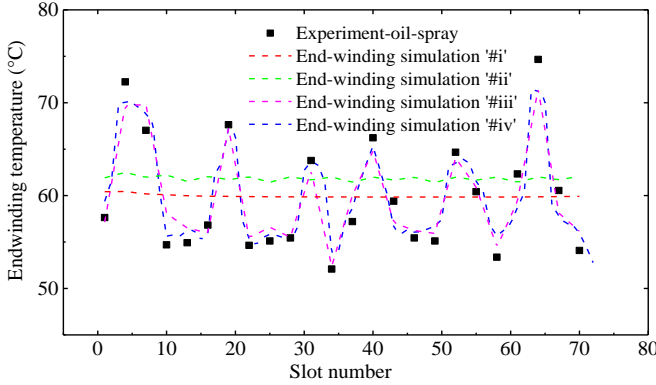


Fig. 13. Temperature comparison with case III for flow rate 1.8 L/min

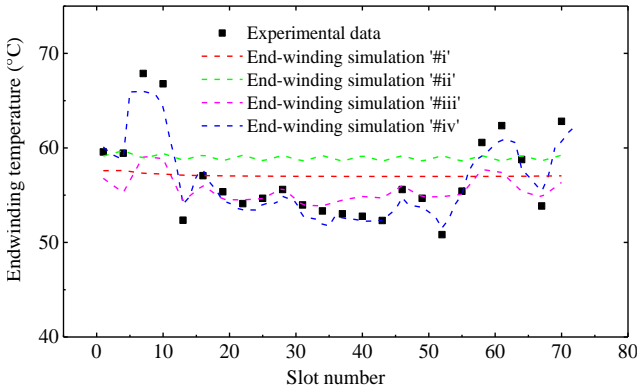


Fig. 14. Temperature comparison with case IV for flow rate 4.5 L/min

TABLE VI summarizes the comparison of the developed LPTN with four different end-winding methodologies to the experimental cases I-IV presented. The error percentage (%) is calculated with (19), where T_{sim} , T_{mea} , T_{oil} are the temperature from the thermal network, the measured temperature, and the oil temperature, respectively.

$$Error = \frac{T_{sim} - T_{mea}}{T_{mea} - T_{oil}} \times 100\% \quad (19)$$

The thermal network with all the end-winding methodologies can predict the average temperature to within 13%, while the peak temperature discrepancy varies significantly amongst the different thermal networks, from an absolute error of less than 1% with methodology '#iv', up to an error of nearly 44% for methodology '#i'. Indeed, the thermal network with end-winding methodologies '#i' and '#ii' cannot predict the uneven temperature distribution. Considering the modified contact area based on the end-winding temperature, the thermal network with end-winding methodology '#iii' is developed, while the 'thick/thin' oil film affect is furtherly added in the thermal network with end-winding methodology '#iv'. Compared to the thermal network with end-winding methodology '#i' and '#ii', the thermal network with end-winding methodology '#iii' provides a more accurate temperature distribution for the full-cone nozzle type. The thermal network with end-winding methodology '#iv' which captures both the oil film thickness as

well as the oil impingent effects, matches well with the measured test values for all the four experimental cases studied. Thus developing thermal networks with end-winding methodology '#iv' can be applied to general hairpin-stator oil-spray cooling arrangements.

TABLE VI. Thermal network comparison with different end-winding methodologies

Case	Tem	Thermal network with end-winding methodology#				Measured	Test rig losses (W)
		i	ii	iii	iv		
Case I	Ave (°C)	51.22 (-7.27%)	51.46 (-5.29%)	52.20 (0.83%)	52.07 (-0.25%)	52.10	349.63
	Peak (°C)	51.79 (-34.5%)	52.47 (-30.72%)	54.89 (-17.3%)	57.78 (-1.22%)	58.00	
Case II	Ave (°C)	53.73 (-1.51%)	54.44 (3.59%)	53.47 (-3.37%)	54.03 (0.63%)	53.94	352.03
	Peak (°C)	54.31 (-43.42%)	57.19 (-32.03%)	60.62 (-18.47%)	64.71 (-2.29%)	65.29	
Case III	Ave (°C)	59.94 (0.71%)	61.85 (10.3%)	59.83 (0.1%)	59.79 (-0.1%)	59.81	359.67
	Peak (°C)	60.44 (-41.03%)	62.50 (-35.08%)	71.51 (-9.09%)	71.33 (-9.61%)	74.66	
Case IV	Ave (°C)	57.08 (1.73%)	58.97 (12.98%)	55.59 (-7.15%)	56.19 (-3.57%)	56.79	355.74
	Peak (°C)	57.61 (-36.81%)	59.71 (-29.28%)	59.12 (-31.4%)	65.98 (-6.78%)	67.87	

For reference TABLE VII lists the convection area coefficient ' β ' value ranges calculated from the measured points. It can be seen that ' β ' range (0.4-1) is similar between cases 'I', 'II' and 'IV', where the nozzle number (12) and nozzles' locations are the same. With case 'III' having a lower nozzle number (6 nozzles), compared to case 'I' and case 'II' (12 nozzles), it can be seen that spray cooling is more effective for higher nozzle numbers as the convection area coefficient is larger. From this table it can be summarized that the convection area coefficient is more sensitive to the number of nozzles and their locations rather than the nozzle type or flow rate.

TABLE VII. Area coefficient ' β ' and heat transfer coefficient values for all four cases

Case	Spray pattern	Nozzle number	Coefficient ' β ' range	
			Lowest	Highest
Case I	full-cone	12 (high flow rate)	0.4897	0.9942
Case II		12 (low flow rate)	0.4229	0.9863
Case III		6	0.2235	0.7857
Case IV	hollow-cone	12	0.4632	0.9999

V. CONCLUSION

Oil-spraying and hairpin windings meld well the manufacturing and thermal management aspects to simultaneously improve the motor's power density and cost-performance. This is placing an immediate need for reference guidelines for the design and analysis of such systems. In this paper a 3D lumped parameter thermal network (LPTN) approach is presented and experimentally validated. While the fundamentals of the LPTN bear similarities to traditional models for random-wound stators with water-jacket cooling, some important particularities need to be considered when modelling oil-sprayed hairpin stators, specifically:

(i) requirement to model the whole machine (360°) rather than using symmetries with half-slot models, in order to capture the non-uniform temperature distribution due to characteristics of sprayed cooling which cause hotspots in the 10 to 2 o'clock positions.

(ii) for consistently accurate modeling on sprayed cooling with different flow rates, nozzle-types, etc., the convection area for heat transfer and the local HTC calculation are proposed in this paper, which take into account the oil-film thickness and impingement effects. For HTC values derivation, an experimental study is the most appropriate methodology available particularly for oil spray cooling on hairpin windings, due to the geometrical complexities and complex spray mechanisms, Tests can be conducted on representative segments at the motor design stage in order to achieve the heat transfer coefficients before manufacturing the full machine prototype.

(iii) use of an individual slot resistance for each slot component, with the number of nodes inside the slot dependent on the hairpin layer number. This is different to traditional random winding systems where an equivalent thermal conductivity is computed based on the material (copper/enamel/resin) composition within the slot.

(iv) importance of maintaining high axial thermal conductivity, while the thermal conductivity of the impregnation resin is less critical than in traditional systems.

(v) in building the LPTN and end-winding thermal resistances for the hairpin winding with sprayed-oil cooling, it is important to understand and follow the same pattern as the electrical connection diagram

The presented guidelines, modeling approach, together with the experimental setup developed should serve as a useful reference for other researchers and practicing engineers modeling this type of motor configuration for the next-generation transport applications.

REFERENCES

- [1] D. Gerada, X. Huang, C. Zhang, H. Zhang, X. Zhang, and C. Gerada, "Electrical machines for automotive electrically assisted turbocharging," *IEEE/ASME Transactions on Mechatronics*, vol. 23, no. 5, pp. 2054-2065, 2018.
- [2] D. Golovanov, L. Papini, D. Gerada, Z. Xu, and C. Gerada, "Multidomain Optimization of High-Power-Density PM Electrical Machines for System Architecture Selection," *IEEE Transactions on Industrial Electronics*, vol. 65, no. 7, pp. 5302-5312, 2018.
- [3] T. Glaessel, D. B. Pinhal, M. Masuch, D. Gerling, and J. Franke, "Manufacturing Influences on the Motor Performance of Traction Drives with Hairpin Winding," in *2019 9th International Electric Drives Production Conference (EDPC)*, 3-4 Dec. 2019 2019, pp. 1-8, doi: 10.1109/EDPC48408.2019.9011872.
- [4] H. Park and M. Lim, "Design of High Power Density and High Efficiency Wound-Field Synchronous Motor for Electric Vehicle Traction," *IEEE Access*, vol. 7, pp. 46677-46685, 2019, doi: 10.1109/ACCESS.2019.2907800.
- [5] D. P. Morisco, H. Rapp, I. L. Iepure, and A. Möckel, "Extended Modelling Approach of Hairpin Winding Eddy Current Losses in High Power Density Traction Machines," in *2020 International Conference on Electrical Machines (ICEM)*, 23-26 Aug. 2020 2020, vol. 1, pp. 874-880, doi: 10.1109/ICEM49940.2020.9270785.
- [6] M. Popescu, J. Goss, D. A. Staton, D. Hawkins, Y. C. Chong, and A. Boglietti, "Electrical Vehicles—Practical Solutions for Power Traction Motor Systems," *IEEE Transactions on Industry Applications*, vol. 54, no. 3, pp. 2751-2762, 2018, doi: 10.1109/TIA.2018.2792459.
- [7] G. Venturini, G. Volpe, M. Villani, and M. Popescu, "Investigation of Cooling Solutions for Hairpin Winding in Traction Application," in *2020 International Conference on Electrical Machines (ICEM)*, 23-26 Aug. 2020 2020, vol. 1, pp. 1573-1578, doi: 10.1109/ICEM49940.2020.9271026.
- [8] A. Reinap, M. Andersson, F. J. Márquez-Fernández, P. Abrahamsson, and M. Alaküla, "Performance Estimation of a Traction Machine with Direct Cooled Hairpin Winding," in *2019 IEEE Transportation Electrification Conference and Expo (ITEC)*, 19-21 June 2019 2019, pp. 1-6, doi: 10.1109/ITEC.2019.8790545.
- [9] L. D. Leonardo, M. Popescu, and M. Villani, "Eddy-Current Losses evaluation in hairpin wound motor fed by PWM Inverter," in *IECON 2020 The 46th Annual Conference of the IEEE Industrial Electronics Society*, 18-21 Oct. 2020 2020, pp. 943-948, doi: 10.1109/IECON43393.2020.9254832.
- [10] T. Dimier, M. Cossale, and T. Wellerdieck, "Comparison of Stator Winding Technologies for High-Speed Motors in Electric Propulsion Systems," in *2020 International Conference on Electrical Machines (ICEM)*, 23-26 Aug. 2020 2020, vol. 1, pp. 2406-2412, doi: 10.1109/ICEM49940.2020.9270943.
- [11] A. Arzillo *et al.*, "Challenges and Future opportunities of Hairpin Technologies," in *2020 IEEE 29th International Symposium on Industrial Electronics (ISIE)*, 2020: IEEE, pp. 277-282.
- [12] G. Berardi and N. Bianchi, "Design Guideline of an AC Hairpin Winding," in *2018 XIII International Conference on Electrical Machines (ICEM)*, 3-6 Sept. 2018 2018, pp. 2444-2450, doi: 10.1109/ICELMACH.2018.8506785.
- [13] M. S. Islam, I. Husain, A. Ahmed, and A. Sathyan, "Asymmetric Bar Winding for High-Speed Traction Electric Machines," *IEEE Transactions on Transportation Electrification*, vol. 6, no. 1, pp. 3-15, 2020, doi: 10.1109/TTE.2019.2962329.
- [14] F. Zhang *et al.*, "Back-Iron Extension Thermal Benefits for Electrical Machines With Concentrated Windings," *IEEE Transactions on Industrial Electronics*, vol. 67, no. 3, pp. 1728-1738, 2020, doi: 10.1109/TIE.2019.2903758.
- [15] S. A. Semidey and J. R. Mayor, "Experimentation of an Electric Machine Technology Demonstrator Incorporating Direct Winding Heat Exchangers," *IEEE Trans. Industrial Electronics*, vol. 61, no. 10, pp. 5771-5778, 2014.
- [16] M. Schiefer and M. Doppelbauer, "Indirect slot cooling for high-power-density machines with concentrated winding," in *2015 IEEE International Electric Machines & Drives Conference (IEMDC)*, 10-13 May 2015 2015, pp. 1820-1825, doi: 10.1109/IEMDC.2015.7409311.
- [17] T. Davin, J. Pellé, S. Harmand, and R. Yu, "Experimental study of oil cooling systems for electric motors," *Applied Thermal Engineering*, vol. 75, pp. 1-13, 2015.
- [18] C. Liu *et al.*, "Experimental Investigation on Oil Spray Cooling With Hairpin Windings," *IEEE Transactions on Industrial Electronics*, vol. 67, no. 9, pp. 7343-7353, 2020, doi: 10.1109/tie.2019.2942563.
- [19] L. Zhenguo, L. Shaoyan, and R. Lin, "The effect of spray parameter on heat dissipation in spray evaporative cooling high power density motors," in *Electrical Machines and Systems (ICEMS), 2017 20th International Conference on*, 2017: IEEE, pp. 1-4.
- [20] J.-y. Jia, Y.-x. Guo, W.-d. Wang, and S.-r. Zhou, "Modeling and experimental research on spray cooling," in *2008 Twenty-fourth Annual IEEE Semiconductor Thermal Measurement and Management Symposium*, 2008: IEEE, pp. 118-123.
- [21] D. Staton, A. Boglietti, and A. Cavagnino, "Solving the more difficult aspects of electric motor thermal analysis in small and medium size industrial induction motors," *IEEE Transactions on Energy Conversion*, vol. 20, no. 3, pp. 620-628, 2005.
- [22] F. Liu, J. Hu, Y. Li, and Q. Wang, "Improved thermal model of forced air-cooled motors considering heat transfer in wire-wound winding and end region," *IET Electric Power Applications*, vol. 14, no. 6, pp. 943-950, 2020, doi: 10.1049/iet-epa.2019.0780.
- [23] A. Tovar-Barranco, A. Lopez-de-Heredia, I. Villar, and F. Briz, "Modeling of End-Space Convection Heat-Transfer for Internal and External Rotor PMSMs with Fractional-Slot Concentrated Windings," *IEEE Transactions on Industrial Electronics*, pp. 1-1, 2020, doi: 10.1109/TIE.2020.2972471.

- [24] S. Nategh, Z. Huang, A. Krings, O. Wallmark, and M. Leksell, "Thermal modeling of directly cooled electric machines using lumped parameter and limited CFD analysis," *IEEE Transactions on Energy Conversion*, vol. 28, no. 4, pp. 979-990, 2013.
- [25] P. Ponomarev, M. Polikarpova, and J. Pyrhönen, "Thermal modeling of directly-oil-cooled permanent magnet synchronous machine," in *2012 XXth International Conference on Electrical Machines*, 2-5 Sept. 2012 2012, pp. 1882-1887, doi: 10.1109/ICEIMach.2012.6350138.
- [26] S. Zhu, M. Cheng, and X. Cai, "Direct Coupling Method for Coupled Field-Circuit Thermal Model of Electrical Machines," *IEEE Transactions on Energy Conversion*, vol. 33, no. 2, pp. 473-482, 2018, doi: 10.1109/TEC.2017.2761787.
- [27] A. Boglietti and A. Cavagnino, "Analysis of the endwinding cooling effects in TEFC induction motors," in *Conference Record of the 2006 IEEE Industry Applications Conference Forty-First IAS Annual Meeting*, 2006, vol. 2: IEEE, pp. 797-804.
- [28] H. Li and Y. Shen, "Thermal Analysis of the Permanent-Magnet Spherical Motor," *IEEE Transactions on Energy Conversion*, vol. 30, no. 3, pp. 991-998, 2015, doi: 10.1109/TEC.2015.2419636.
- [29] N. Simpson, R. Wrobel, and P. H. Mellor, "A General Arc-Segment Element for Three-Dimensional Thermal Modeling," *IEEE Transactions on Magnetics*, vol. 50, no. 2, pp. 265-268, 2014, doi: 10.1109/TMAG.2013.2278866.
- [30] O. Wallscheid and J. Böcker, "Global Identification of a Low-Order Lumped-Parameter Thermal Network for Permanent Magnet Synchronous Motors," *IEEE Transactions on Energy Conversion*, vol. 31, no. 1, pp. 354-365, 2016, doi: 10.1109/TEC.2015.2473673.
- [31] R. Wrobel and P. Mellor, "A general cuboidal element for three-dimensional thermal modelling," *IEEE Transactions on Magnetics*, vol. 46, no. 8, pp. 3197-3200, 2010.
- [32] P. Mellor, D. Roberts, and D. Turner, "Lumped parameter thermal model for electrical machines of TEFC design," in *IEE Proceedings B-Electric Power Applications*, 1991, vol. 138, no. 5: IET, pp. 205-218.
- [33] D. Gerling and G. Dajaku, "Thermal calculation of systems with distributed heat generation," in *Thermal and Thermomechanical Proceedings 10th Intersociety Conference on Phenomena in Electronics Systems, 2006. ITherm 2006.*, 2006: IEEE, pp. 8 pp.-652.
- [34] D. Gerling and G. Dajaku, "Novel lumped-parameter thermal model for electrical systems," in *2005 European Conference on Power Electronics and Applications*, 2005: IEEE, pp. 10 pp.-P. 10.
- [35] C. Noerenberg, J. Redlich, and B. Ponick, "Novel method for considering AC copper losses in traction motors," in *2020 International Conference on Electrical Machines (ICEM)*, 23-26 Aug. 2020 2020, vol. 1, pp. 947-953, doi: 10.1109/ICEM49940.2020.9271008.
- [36] H. Vansompel and P. Sergeant, "Extended End-Winding Cooling Insert for High Power Density Electric Machines with Concentrated Windings," *IEEE Transactions on Energy Conversion*, pp. 1-1, 2019, doi: 10.1109/TEC.2019.2953577.
- [37] D. A. Staton and A. Cavagnino, "Convection Heat Transfer and Flow Calculations Suitable for Electric Machines Thermal Models," *IEEE Transactions on Industrial Electronics*, vol. 55, no. 10, pp. 3509-3516, 2008, doi: 10.1109/TIE.2008.922604.

APPENDIX

L – Stator length	M – Axial sections number	N – Slot number	r_1 – Stator inner radius
r_2 – Lower layer radius	r_3 – Upper layer radius	r_4 – Slot bottom radius	r_5 – Stator back-iron radius
r_6 – Stator outer radius	r_7 – Frame radius	a_1 – Pin dimension - hori	b_1 – Pin dimension – vert
a_2 – Slot width – hori	b_2 – Slot depth – vert	δ_0 – Copper insulation thickness	
δ_1 – Slot liner thickness		δ_2 – Impregnation thickness - thin	
δ_3 – Impregnation thickness - thick		δ_4 – Equivalent air-gap thickness between frame and core	
c – Stator back-iron width - average		λ_0 – Copper insulation thermal conductivity	
λ_1 – Copper thermal conductivity		λ_2 – Impregnation thermal conductivity	
λ_3 – Slot liner thermal conductivity		λ_4 – Lamination radial thermal conductivity	

λ_5 – Lamination axial thermal conductivity

λ_7 – Air thermal conductivity

h_2 – Heat transfer coefficient on the spray-side for the studied slot

β – convection area coefficient for the studied slot

K – the end-winding height on the thermally-insulated side

λ_6 – Frame thermal conductivity

h_1 – Natural convection heat transfer coefficient

h_3 – Heat transfer coefficient on the thermally-insulated side

H – the end-winding height on the sprayed side

d – slots number the end-winding crossing

A. Radial thermal resistances

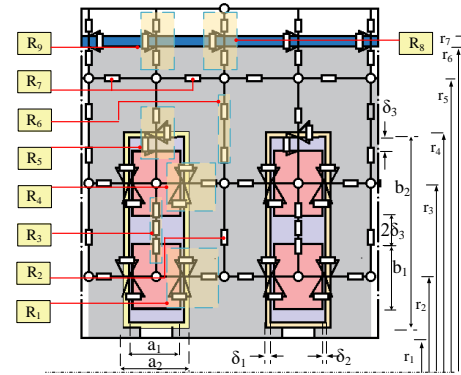


Fig. 15. Thermal resistance in radial direction

There are two types of radial thermal resistance calculation formulas in this section, (i) it consists of different components with various thermal conductivities: R_1 calculation is applied in this case with thermal resistance in copper, wire insulation, impregnation resin, slot liner and tooth; (ii) it is single component thermal resistance calculation, such as R_2 with only tooth thermal resistance.

$$R_1 = \frac{\frac{a_1}{2}}{\lambda_1 \left(\frac{L}{M}\right) b_1} + \frac{\delta_0}{\lambda_0 \left(\frac{L}{M}\right) b_1} + \frac{\delta_2}{\lambda_2 \left(\frac{L}{M}\right) b_1} + \frac{\delta_3}{\lambda_3 \left(\frac{L}{M}\right) b_1} + \frac{\frac{\pi r_2}{N} - \frac{a_2}{2}}{\lambda_4 \left(\frac{L}{M}\right) \left(\frac{b_2}{2}\right)} \quad (20)$$

$$R_2 = \frac{r_3 - r_2}{\lambda_4 \left(\frac{L}{M}\right) \left(\frac{\pi(r_2 + r_3)}{N} - a_2\right)} \quad (21)$$

$$R_8 = \frac{r_6 - r_5}{\lambda_4 \left(\frac{L}{M}\right) \left(\frac{\pi(r_5 + r_6)}{N} - a_2\right)} + \frac{\delta_4}{\lambda_7 \left(\frac{L}{M}\right) \left(\frac{2\pi r_6}{N} - a_2\right)} + \frac{r_7 - r_6}{\lambda_6 \left(\frac{L}{M}\right) \left(\frac{\pi(r_6 + r_7)}{N} - a_2\right)} + \frac{1}{h_1 \left(\frac{L}{M}\right) \left(\frac{2\pi r_7}{N} - a_2\right)} \quad (22)$$

In Fig. 15, thermal resistance R_3, R_4, R_5, R_6 calculation process is similar to R_1 ; R_7 calculation is similar to R_2 ; while R_9 calculation is similar to R_8 .

B. Axial thermal resistances and the end-winding region

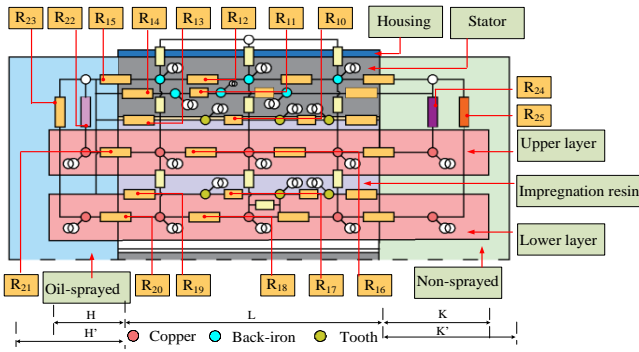


Fig. 16. Thermal resistance axially and in the end-winding

B.1 Axial thermal resistances

Axial thermal resistance in the core part only consists of one component with single thermal conductivity. Formula (23) is presented as an example to calculate the copper thermal resistance R_{16} between two axial planes. $R_{10}, R_{11}, R_{12}, R_{17}, R_{18}$ use a similar formula.

$$R_{16} = \frac{L}{\lambda_1 M} \quad (23)$$

Axial thermal resistance R_{20} between the core machine and the end-winding region is calculated with (24), which can also be used to calculate R_{21} .

$$R_{20} = \frac{L}{\lambda_1} \left(\frac{1}{2M} + \frac{H}{2} \right) \quad (24)$$

B.2 Convection thermal resistances in the end-winding region

The convection thermal resistance calculation formula between the stator and the fluid in the end-winding region consists of two parts, axial conduction thermal resistance and convection thermal resistance. Formulas (25) and (26) are used as an example to calculate the thermal resistance R_{19} between the tooth and the fluid in the end-winding region. Similar formulas can be extracted easily to calculate R_{13}, R_{14}, R_{15} .

$$S_{19} = \frac{\pi((r_2 + \delta_0 + \delta_3 + b_1/2)^2 - r_1^2)}{N} - \frac{a_2 b_2}{2} \quad (25)$$

$$R_{19} = \frac{L}{\lambda_5 S_{19}} + \frac{1}{h_2 S_{19}} \quad (26)$$

The convection thermal resistance calculation between the winding and the fluid is complicated as there are four surfaces in contact with the fluid. Formulas (27), (28) and (29) are used to calculate R_{22} in Fig. 16. R_{23}, R_{24}, R_{25} can be calculated with similar formulas.

$$R_{22-1} = \frac{\frac{a_1}{2}}{\lambda_1(H+3c)b_1} + \frac{\delta_0}{\lambda_0(H+3c)b_1} \quad (27)$$

$$R_{22-2} = \frac{\frac{b_1}{2}}{\lambda_1(H+3c)a_1} + \frac{\delta_0}{\lambda_0(H+3c)a_1} \quad (28)$$

$$R_{22} = \frac{R_{22-1}R_{22-2}}{R_{22-1} + R_{22-2}} + \frac{1}{h_2\beta(H+3c)(2a_1+2b_1)} \quad (29)$$

C. Connection thermal resistance between different slot

As mentioned in section IIA, a thermal model for the full stator is built, with thermal resistance connecting different slots. Formula (30) is used to calculate the axial thermal resistance between two slots (crossing 'd' slots) on the oil-sprayed side, as shown in Fig. 17. Similar formula can be obtained on the non-sprayed side.

$$R_{26} = \frac{H+cd}{\lambda_1(a_1b_1)} \quad (30)$$

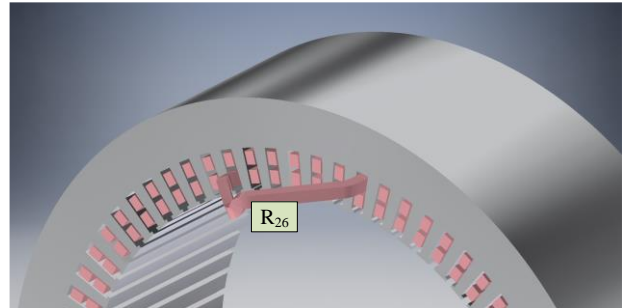


Fig. 17. Connection thermal resistance



Fengyu Zhang received B.E degree in thermal engineering from Huazhong University of Science and Technology, Wuhan, China in 2014 and Ph.D. degree in electrical machines from University of Nottingham in 2019. She is currently a Research Fellow in the area of thermal management on electrical machines within the PEMC group at University of Nottingham. Her main research interests include high performance motors for transport applications and their multi-domain optimization.



David Gerada received the Ph.D. degree in high-speed electrical machines from University of Nottingham, Nottingham, U.K., in 2012.

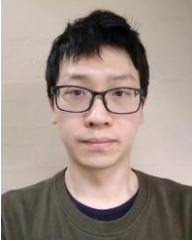
From 2007 to 2016, he was with the R&D Department at Cummins, Stamford, U.K., first as an Electromagnetic Design Engineer (2007–2012), and then as a Senior Electromagnetic Design Engineer and Innovation Leader (2012–2016). At Cummins, he pioneered the design and development of high-speed electrical machines, transforming a challenging technology into a reliable one suitable for the transportation market, while establishing industry-wide-used metrics for such machinery. In 2016, he joined the University of Nottingham where he is currently a Principal Research Fellow, responsible for developing state-of-the-art electrical machines for future transportation which push existing technology boundaries, while propelling the new technologies to higher technology readiness levels.

Dr. Gerada is a Chartered Engineer in the U.K. and a member of the Institution of Engineering and Technology.



Zeyuan Xu received the Ph.D. degree in mechanical engineering from the University of Manchester, Manchester, U.K., in 2002.

He subsequently worked as a Research Fellow at UMIST, Brunel University, and University of Nottingham. He is currently a Senior Research Fellow in thermo-mechanical design of high speed electrical machines within the PEMC group at University of Nottingham, Nottingham, U.K. His main research interests include turbulent thermo-fluid flow, heat transfer enhancement, and thermal management of advanced electrical machines and power electronics.



Chuan Liu received his B.E. degree in mechanical engineering from Nanjing Agricultural University, Nanjing, China, in 2015, and his Ph.D. degree in electrical and electronic engineering with the University of Nottingham, UK.

In 2015, he was a Research Assistant on Electrical Machine Design and Manufacture with the University of Nottingham Ningbo China. Since his graduation in 2020, he has been working as a knowledge transfer associate for a partnership between Motor Design Ltd. and the University of Nottingham. The knowledge transfer partnership aims to develop fast and accurate modelling capability to simulate and design oil spray cooling systems for the next generation of electric traction motors.



He Zhang received his B.Eng. degree from Zhejiang University, China, in 2002. He obtained the MSc. and Ph.D. degree in electrical machines from The University of Nottingham, UK, in 2004 and 2009 respectively. After this he worked as Research Fellow at the University and Director of BestMotion Technology Centre. He moved to University of Nottingham Ningbo China as Senior Research Fellow in 2014, promoted to Principal Research Fellow in 2016 and to Professor in 2020.

Currently he is the Director of Nottingham Electrification Centre (NEC) within the Power electronics, Machines and Control research group in University Of Nottingham. His research interests include high performance electric machines and drives for transport electrification.



Tianjie Zou (S'15-M'18) was born in Hubei, China, in 1991. He received the B.Sc. degree in 2013 in electrical and electronic engineering, and Ph.D. degree in electrical engineering in 2018, both from Huazhong University of Science and Technology, Wuhan, China.

He joined the University of Nottingham, U.K., in 2018, as a research fellow within the Power Electronics, Machines and Control (PEMC) Group. In 2020, he was awarded Nottingham Research Fellowship and started his independent research career. His main research interests include design, analysis, and intelligent control of permanent-magnet machines. Dr. Zou was the recipient of the Best Paper Award in the 22nd International Conference on Electrical Machines (ICEM 2016).



Yew Chuan Chong (Eddie) received Ph.D. degree in 2015 from the University of Edinburgh, Edinburgh, U.K. He joined Motor Design Ltd. UK (MDL) as a Senior Research Engineer in January 2014. Currently he is the Technical Lead (Asia) of the MDL office in Shanghai China, managing with both technical and commercial functions in the Asia market and leading thermal aspects of research/consultancy projects and Motor-CAD software development. His major research area is improving algorithms for thermo-

fluid modelling in electrical machines, and effectively make use of lumped parameter thermal network, flow network, finite element and computational

fluid dynamic (CFD) methods for thermal management of electrical machine and to improve the cooling of electrical machines.



Chris Gerada (SM'12) is an Associate Pro-Vice-Chancellor for Industrial Strategy and Impact and Professor of Electrical Machines. His principal research interest lies in electromagnetic energy conversion in electrical machines and drives, focusing mainly on transport electrification. He has secured over £20M of funding through major industrial, European and UK grants and authored more than 350 referred publications. He received the

Ph.D. degree in numerical modelling of electrical machines from The University of Nottingham, Nottingham, U.K., in 2005. He subsequently worked as a Researcher with The University of Nottingham on high-performance electrical drives and on the design and modelling of electromagnetic actuators for aerospace applications. In 2008, he was appointed as a Lecturer in electrical machines; in 2011, as an Associate Professor; and in 2013, as a Professor at The University of Nottingham. He was awarded a Research Chair from the Royal Academy of Engineering in 2013. Prof. Gerada served as an Associate Editor for the IEEE TRANSACTIONS ON INDUSTRY APPLICATIONS and is the past Chair of the IEEE IES Electrical Machines Committee.